NASA TECHNICAL MEMORANDUM 100540

A FIBER-RESIN MICROMECHANICS ANALYSIS OF THE DELAMINATION FRONT IN A DCB SPECIMEN

J. H. Crews, Jr., K. N. Shivakumar, and I. S. Raju

JANUARY 1988

NASA
National Aeronautics and
Space Administration

Langley Research Center
Hampton, Virginia 23665

INTRODUCTION

Many current composites are made with rather brittle thermoset resins and have low interlaminar fracture toughness. As a result, these laminates are easily damaged. An understanding of the interaction between the fibers and the resin during interlaminar fracture could provide useful guidelines for developing tougher composite systems. The purpose of this study was to contribute to this understanding through an analysis of the delamination front in a double cantilever beam (DCB) specimen. The DCB specimen has been widely used to characterize the mode I interlaminar fracture toughness of laminates. Several experimental [1-6] and analytical [7-11] studies have been conducted to analyze the fracture mechanism and factors influencing fracture. The effects of adherend configuration and material properties on the stress distribution and the strain-energy-release rate were investigated in references 5, 8, and 10. The influence of adhesive thickness on the amount of yielding ahead of the delamination front was also explored in reference 10.

In the analyses reported to date, the DCB specimen has been modeled as two homogeneous, orthotropic adherends with or without a resin interface layer. No attempt has been made to examine the stress state within the adherend by modeling the fibers and resin separately. The present study addresses this need by analyzing a DCB specimen using a fiber and resin micromechanics model of a small region at the delamination front. A three-dimensional (3D) model [11] of the complete DCB specimen with homogeneous material properties was analyzed to determine the boundary conditions for the local fiber-resin model. The present study had the following objectives: (1) to model the delamination region of a DCB specimen, representing discrete fibers and resin, (2) to analyze the stresses within this fiber-resin model, and (3) to estimate the extent of yielding in the resin.

The local model had a height of one ply thickness and extended a little more than one ply thickness ahead of and behind the delamination front. The fiber-resin portion of the local model contained four fibers and surrounding resin, with a thin "resin-rich" interface layer, typical of cocured graphite/epoxy laminates. The remainder of the local model was homogeneous. A finite element analysis with twenty-noded, 3D, parabolic elements was used. The displacements calculated from the 3D analysis of an orthotropic DCB specimen [11] were imposed as boundary conditions on the local model.

Stress components within the fiber-resin region were calculated and stress distributions are presented along selected planes and surfaces within the local fiber-resin model. Yielding in the resin interface layer and the fiber-resin region was estimated using computed elastic stresses with the von Mises and a modified von Mises yield criteria. The modified von Mises yield criterion accounted for hydrostatic stress effects. The extent of yielding in the composite DCB specimen was also compared with that from an all-resin DCB specimen.

LIST OF SYMBOLS

a	delamination length, m
E_r	Young's modulus of resin, GPa
G_I	strain-energy-release rate (mode I), J/m^2
G_{Ic}	delamination fracture toughness, J/m^2
h	ply thickness, m
K_I	stress-intensity factor (mode I), $N/m^{3/2}$
P	applied load, N/m
r, θ, x	fiber cylindrical coordinates, m, deg, m
t	thickness of resin interface layer, m

u, v, w	displacements in x-, y-, and z-directions, respectively, m
v_δ	opening displacement of first quarter-point node behind delamination front, m
w	specimen width, m
x, y, z	Cartesian coordinates, m
ν_r	Poisson's ratio of resin
σ_r, $\sigma_{r\theta}$, σ_{rx}	fiber-resin interface stresses, MPa
σ_x, σ_y, σ_z	resin normal stresses, MPa

ANALYSIS

The 3D analysis of a DC specimen [11] showed that the stress state was nearly uniform along the delamination front except near the specimen edges. As a result, the delamination stresses can be studied by examining a typical interior "slice" of the specimen. Details of the analysis are presented in this section.

Specimen Configuration and Materials

Figure 1(a) shows the DCB specimen consisting of two cocured adherends with a resin interface layer 10 μm thick. Each adherend represents a 12-ply unidirectional graphite/epoxy laminate 1.65 mm thick. The delamination, located in the middle of the resin interface layer, has a length a of 50.8 mm and width w of 25.4 mm. The elastic properties used for the fiber, resin, and graphite/epoxy lamina are given in Table 1. The resin and lamina properties were taken from reference 11 and used in micromechanics equations [12] to calculate the fiber properties by iteration. The specimen is loaded as shown, by imposing uniform displacements in the y-direction. The

3

corresponding load per unit width is denoted as P. Unless otherwise specified, the results in this report correspond to P = 1 N/m.

Local Region Modeling

Figure 1(a) also shows a small 3D, rectangular region at the delamination front. This small region represents a typical slice of the DCB interior. As shown in figure 1(b), this local region is sub-divided into a fiber-resin region and a homogeneous orthotropic region. The elastic properties of the homogeneous region were the same as used in the global DCB model. The local model has a height of about one ply thickness (135 μm) and extends 165 μm behind and ahead of the delamination front.

For simplicity, the fibers were arranged in a regular square array [13] with a fiber volume fraction of 0.63, typical of graphite/epoxy laminates. For a typical fiber diameter of 7 μm, the center distance between adjacent fibers was 8 μm. Figure 2(a) shows the arrangement of fibers in the fiber-resin region. Due to symmetry, only half of each fiber was modeled, giving a model thickness of 4 μm. Computational limitations restricted the number of fibers to four. Thus, the fiber-resin region was 37 μm high and extended 80 μm behind and 165 μm ahead of the delamination front. For convenience, the same finite element mesh was used for all x = constant planes (including the homogeneous, orthotropic portion of the local model). Also, the mesh refinement behind the delamination front was a mirror image of the mesh ahead of the front. The mesh refinement at the delamination front is shown in figure 2(b). In the collapsed elements at the delamination front, the mid-side nodes were moved to the quarter points [14, 15] to produce a stress field with a square root singularity. The size of the collapsed elements was 0.05 μm.

4

Several analyses were performed by varying the mesh refinement in the x-direction and in the y-z plane. Stresses along the delamination plane were compared with each other and with the fine-mesh, 2D results from reference 10. A 3D, coarse mesh with 1892 elements and 10,670 nodes was found to adequately describe the singular stress distribution ahead of the delamination. However, this coarse mesh did not give smooth stress distributions in the width (z) direction. This problem was solved by refining the mesh in the y-z plane to obtain the model used throughout this study. This model, shown in figure 2, had 4578 elements and 23,037 nodes with 69,111 degrees of freedom.

Boundary Conditions for the Local Model

The stress analysis of the local model was performed by imposing nodal displacements on the faces of the model (except at the delamination plane). As previously mentioned, these displacements were calculated from the 3D analysis of the DCB specimen in reference 11. On the back face of the model $(z = 0)$, the w-displacements were set equal to zero. On the delamination plane $(y = 0)$, the stresses were zero behind the delamination front and the v-displacements were zero ahead of it. A brief description of the other boundary displacement conditions is given in Appendix A.

Strain-Energy-Release Rate Computation

The crack-opening-displacement method was used to calculate the stress-intensity factor K_I and then the strain-energy-release rate G_I was calculated from K_I. Assuming the stress state at the delamination front was nearly plane strain, the equation for the stress-intensity factor is given by

$$K_I = \frac{E_r v_\delta}{4(1 - \nu_r^2)} \sqrt{\frac{2\pi}{\delta}} \tag{1}$$

where v_δ is the opening displacement at the first quarter-point node ($\delta = 0.0125 \ \mu m$) behind the delamination front. This v_δ is one-half the crack opening displacement. The constants E_r and ν_r represent the resin layer elastic modulus and Poisson's ratio, respectively. The strain-energy-release rate G_I is obtained from K_I using the following equation

$$G_I = \frac{(1 - \nu_r^2)K_I^2}{E_r} \tag{2}$$

RESULTS AND DISCUSSION

The formulation of the local model was evaluated by performing an analysis of the local region, assuming it to be homogeneous and orthotropic, and then comparing these results with the 3D analysis of the DCB specimen [11]. The calculated stress distributions ahead of the delamination front from the two analyses were nearly identical. The value of G_I calculated from the local analysis was 0.592×10^{-4} J/m^2, which agreed very well with 0.597×10^{-4} J/m^2 for the mid-section of the delamination front from reference 11.

Stresses in the Interlaminar Resin Layer

Figure 3, taken from reference 11, shows the distributions of the σ_x, σ_y, and σ_z stresses along the x-axis in the resin layer ahead of the delamination front. This figure shows the very high stresses and stress gradients immediately ahead of the delamination front. Of the three stress components, σ_y is dominant; hence, the following discussions will focus on this stress.

Figure 4 shows the σ_y distribution ahead of the delamination front calculated from the local region analysis. A logarithmic scale was chosen to emphasize the region close to the delamination front. The stress distributions at $z = 0$ and $z = 4$ μm are virtually identical. Both stress distributions show the characteristic slope of -1/2 very near delamination front and have shapes similar to that of curves from the 2D analyses in references 7 and 10. Hence, the fibers modeled discretely in the present analysis did not influence the stresses along the x-axis ahead of the delamination.

Figure 5 shows σ_y stress distributions in the resin layer immediately above the delamination front. These distributions are in the $x = 0$ plane along lines parallel to the delamination front. Very close to the delamination front, $y = 0.75$ μm, the σ_y stress is nearly constant over the model thickness. Farther away from the delamination, the σ_y stresses are lower, as expected, but are slightly elevated near the fiber centerline ($z = 4$ μm). The load path through the fibers is stiffer than along a parallel path through the resin; therefore, the σ_y stress is elevated under the fiber. However, as figure 5 shows, this trend dissipated within the resin layer. As a result, the σ_y stress is virtually constant along the delamination front

7

over the interior portion of the DCB specimen represented by this fiber-resin model.

Strain-Energy-Release Rate

Figure 6 compares the values of the strain-energy-release rate G_I along the delamination front for three models of the DCB specimen: (1) a 2D plane strain model [10], (2) a 3D homogeneous, orthotropic model [11], and (3) the present fiber-resin model. For the fiber-resin model, G_I at the fiber centerline is only about two percent higher than at $z = 0$. This G_I distribution is nearly constant because σ_y varied very little along the delamination front, as shown in figure 5. The average G_I for the fiber-resin model is $0.564 \times 10^{-4} J/m^2$. This is about seven percent lower than the 3D value of $0.597 \times 10^{-4} J/m^2$ for the specimen midplane [11]. The average value for the fiber-resin model is only about four percent lower than the 2D plane-strain value of $0.570 \times 10^{-4} J/m^2$ [10].

Ply Stresses

Figure 7 shows the σ_y stress versus z through the fiber-resin model. The solid curve, from figure 5, is the stress distribution at the "interface" between the ply and the resin layer. The other three curves represent the σ_y distributions midway between the fibers. For each curve, the σ_y stress is highest where the fibers are closest together, at the fiber centerline ($z = 4$ μm). Also, as expected, the σ_y stresses decrease as y increases away from the delamination.

Figure 8(a) shows σ_x resin stress distributions in the $x = 0$ plane. The dashed curves represent the σ_x stresses for $z = 0$ (the y-axis) and the solid curve segments represent σ_x stresses for $z = 4$ μm (the centerline

through the fibers). For comparison, the σ_x stress distribution for an all-resin model is also shown. For z = 0, the dashed σ_x curve varies in a cyclic manner and is lower than the σ_x curve for the all-resin model. However, the solid curve segments for z = 4 μm are higher than the all-resin (dash-dot) curve, except near the delamination front. The fibers produce σ_x stress concentrations in the resin where the fibers are closest together. Figure 8(b) shows similar σ_y stress distributions. Again, the solid curve segments for z = 4 μm are much higher than the dash-dot curve for the all-resin case, indicating a significant σ_y stress concentration between the fibers. Figure 8(c) shows similar σ_z stress concentrations between the fibers. These local stress concentrations will be discussed later in terms of their influence on resin yielding near the delamination front.

Fiber-Resin Interface Stresses

To examine the stresses at the fiber-resin interfaces, cylindrical coordinates were used for each fiber. As shown in figure 9, r, θ, and x represent the radial, circumferential, and axial fiber directions. The interfacial stress state consists of a radial stress σ_r and two shear stresses $\sigma_{r\theta}$ and σ_{rx}, as shown. Figure 9 shows the interface stress distributions for the first fiber above the delamination front (in the x = 0° plane). This is the most highly stressed portion of the fiber-resin interface. As expected, the σ_r stress has peak values at θ = 0° and 180° and a minimum at θ = 90°. Because of symmetry, $\sigma_{r\theta}$ is zero at θ = 0° and 180°. This dashed curve changes sign near θ = 90° and has peaks near 45° and 160°. The σ_{rx} distribution has peaks at 0° and 180° and changes sign near θ = 90°.

9

Next, each of the three curves discussed in figure 9 is compared with its counterparts for the other three fibers. Figures 10(a), (b) and (c) compare the σ_r, $\sigma_{r\theta}$, and σ_{rx} stresses, respectively, for the four fibers. These curves have similar shapes, with the expected lower magnitudes for fibers farther from the delamination front.

Distributions of the interface stresses σ_r and σ_{rx} at $\theta = 0$ along the first fiber are shown in Figure 11. The normal stress σ_r reaches a peak just ahead of the delamination front (at $x = 0$) and then rapidly decreases. The shear stress σ_{rx} has its maximum value slightly behind the delamination front and changes sign ahead of the delamination front before decreasing to zero. Since the fiber-resin interfaces near the delamination front are subjected to combined normal and shear stresses, interfacial strength and toughness analyses will, therefore, probably require multi-axial stress criteria.

Yielding Near the Delamination Front

The computed elastic stresses were used with the von Mises yield criterion to estimate the region of resin yielding near the delamination front. The stresses used in calculating the yield zone were found by scaling the load until G_I was equal to G_{IC} and, therefore, corresponded to the incipient delamination growth condition. However, because this procedure uses elastic stresses and does not account for stress redistribution due to yielding, the resulting yield zone estimates should be smaller than actual values. The yield zone for the fiber-resin model was compared with that for a all-resin DCB specimen loaded to the same G_I condition. Also, yield zones were compared using the von Mises yield criterion and a modified von Mises criterion that includes hydrostatic stress effects.

Figure 12 shows calculated yield zones based on the von Mises yield criterion for a load level corresponding to $G_I = 85$ J/m^2 (a typical G_{Ic} for a brittle graphite/epoxy composite [2]). This rather low value of G_{Ic} was selected so that yielding did not develop beyond the fiber-resin portion of the local model. Figure 12(a) shows a cross-section at $x = 0$ and 12(b) shows the front surface of the model ($z = 4$ μm). The expected yielding in the interlaminar resin layer ahead of the delamination was found. However, localized yielding was also found between adjacent fibers. As indicated previously (figure 8), these regions have resin stress concentrations. A 2D, finite element analysis of an all-resin DCB specimen was performed for a load corresponding to $G_I = 85$ J/m^2. The yield zone height was found to be less than the thickness of the interlaminar resin layer in the fiber-resin model. A comparison of the yield zones in the fiber-resin model and the all-resin model showed that the yielded volume in the fiber-resin model was about 3.5 times that for the all-resin case. The resin stress concentrations caused by fibers increased yielding compared to the all-resin case. This contradicts the widely held assumption that fibers restrict yielding at a delamination and, therefore, cause a smaller yield zone than in a corresponding all-resin case. Of course, the present procedures provide only approximate yield zones and the cases compared represent rather brittle materials ($G_{Ic} = 85$ J/m^2).

Because yielding contributes to fracture toughness G_{Ic}, the present yield zone comparison may provide another explanation for the observation in reference 2 that G_{Ic} for a DCB specimen can be twice as large as that for an all-resin specimen. This unexpected observation was explained in reference 2 by fiber bridging effects that can elevate the interlaminar toughness compared to the all-resin value. The effective height of the yield zone estimated for the present fiber-resin case was found to be about twice that for the

11

corresponding all-resin case. Thus, the present comparison may be quantitatively significant; however, it is limited to rather brittle materials and cannot address the important trends shown in reference 2 for tough resins and composites.

The yielding of thermoplastic polymers has been shown to be influenced by the hydrostatic component of the stress state [16-20]. In the present problem, the stress state near the delamination front was found to have a significant hydrostatic tension component. For thermoplastic resins this can increase yielding compared to that predicted by the von Mises criterion. Although the present analysis used elastic material properties and a G_{Ic} that represented a thermoset resin, the computed stress distributions should be similar to those for a thermoplastic resin. Therefore, a modified von Mises criterion (Appendix B), which includes the hydrostatic stress component, was used to obtain a second estimate the yield zone. This calculated yield zone, again corresponding to $G_I = 85$ J/m^2, is shown in figure 13. A comparison of figures 12 and 13 shows a significant increase in the size of the yield zone due to the hydrostatic stress effect.

CONCLUDING REMARKS

A 3D finite element model was developed to analyze the fiber-resin interaction at the delamination front in a double cantilever beam (DCB) specimen. This model represented a small portion of a graphite/epoxy ply as well as one-half of the thin resin interface layer with the delamination at the DCB specimen midplane. Within this model, the fibers were arranged in a square array with a fiber volume fraction of 0.63. Resin stress distributions, fiber-resin interface stress distributions, strain-energy-release rates, and resin yielding were analyzed.

1. Within most of the interlaminar resin layer, the delamination opening mode stress σ_y was nearly uniform across the specimen interior. This σ_y stress was slightly higher in the region where the fiber was closest to the delamination.

2. The fiber had a small influence on the delamination strain-energy-release rate G_I, which varied by only about two percent because of the fiber. The average G_I value for the fiber-resin model was about four percent smaller than the 2D, plain strain value for an equivalent homogeneous, orthotropic DCB specimen.

3. Near the delamination front, the fiber-resin interfaces were subjected to combined normal and shear stresses that varied around and along the fibers. These results suggest that a multi-axial stress criterion may be required to analyze the fiber-resin interface strength or toughness.

4. Resin stress concentrations were found between the fibers. These stress concentrations produced localized, fiber-induced yield zones between the fibers. The volume of the estimated equivalent yield zone for this fiber-resin model was larger than that for a corresponding all-resin DCB model loaded to the same G_I level. This suggests that the fibers can increase the extent of matrix yielding associated with delamination growth and may, therefore, increase fracture toughness, rather than restrict it as usually assumed.

5. The stress analysis indicated a significant hydrostatic tensile stress near the delamination front. When a modified von Mises yield criterion was used to account for the hydrostatic stress, larger yield zones were estimated for the delamination front. Thus the effects of hydrostatic stress on yielding onset and subsequent inelastic deformation should be included in

future DCB specimen analyses. This should be especially important for resins that craze under the influence of hydrostatic tensile streses.

REFERENCES

1. Wilkins, D. J.; Eisenmann, J. R.; Camin, R. A.; and Margolis, W. S.: "Characterizing Delamination Growth in Graphite/Epoxy," Damage in Composite Materials: Basic Mechanisms, Accumulation, Tolerance, and Characterization, ASTM STP 775, K. L. Reifsnider, Ed., American Society for Testing and Materials, 1982, p. 168.

2. Hunston, D. L.: "Composite Interlaminar Fracture: Effect of Matrix Fracture Energy," Journal of Composite Technology Review, Vol. 6, No 4, Winter 1984, pp. 176-180.

3. Chai, H.: "Bond Thickness Effect in Adhesive Joints and Its Significance for Mode I Interlaminar Fracture of Composites," Composite Materials: Testing and Design (Seventh Conference), ASTM STP 893, J. M. Whitney, Ed., American Society for Testing and Materials, 1986, pp. 209-231.

4. Johnson, W. S.; and Mangalgiri, P. D.: "Investigation of Fiber Bridging in Double Cantilever Beam Specimens," NASA TM-87716, April 1986.

5. Mangalgiri, P. D.; Johnson, W. S.; and Everett, R. A.,Jr.: "Effect of Adherend Thickness and Mixed Mode Loading on Debond Growth in Adhesively Bonded Composite Joints," NASA TM-88992, September 1986.

6. Bradley, W. L.; and Cohen, R. N.: "Matrix Deformation and Fracture in Graphite Reinforced Epoxies," Delamination and Debonding of Materials, STP 876, W. S. Johnson, Ed., American Society of Testing and Materials, 1985, pp. 389-410.

7. Wang, S. S.; Mandell, J. F.; and McGarry, F. J.: "An Analysis of the Crack Tip Stress Field in DCB Adhesive Fracture Specimens," Int. Journal of Fracture, Vol. 14, No. 1, Feb. 1978, pp. 39-58.

8. Hunston, D. L.; Kinloch, A. J.; Shaw, S. J.; and Wang, S. S.: "Characterization of Fracture Behavior of Adhesive Joints, "Proceedings

Int. Symposium on Adhesive Joints, K. L. Mittal, Ed., September 1982, pp. 789-808.

9. Whitney, J. M.: "Stress Analysis of the Double Cantilever Beam Specimen," Composite Science and Technology, Vol. 23, 1985, pp. 201-219.

10. Crews, J. H., Jr.; Shivakumar, K. N.; and Raju, I. S.: "Factors Influencing Elastic Stresses in Double Cantilever Beam Specimens," NASA TM-89033, November 1986.

11. Raju, I. S.; Shivakumar, K. N.; and Crews, J. H., Jr.: "Three-Dimensional Elastic Analysis of a Composite Double Cantilever Beam Specimen," AIAA/ASME/ASCE/AHS 28th Structures, Structural Dynamics, and Materials Conference, Monterey, CA, AIAA Paper 87-0864, April 6-8, 1987.

12. Kriz, R. D.; and Stinchcomb, W. W.: "Elastic Moduli of Transversely Isotropic Fibers and Their Composites," Experimental Mechanics, Vol. 19, 1979, p. 41.

13. Herrmans, L. R.; and Pister, K. S.: "Composite Properties of Filament-Resin Systems," ASME Paper 63-WA-239, Presented at the ASME Winter Annual Meeting, Philadelphia, PA, Nov. 17-23, 1963.

14. Barsoum, R. S.: "On the Use of Isoparametric Finite-Elements in Linear Fracture Mechanics," Int. Journal of Numerical Methods in Engineering, Vol. 10, 1976, pp. 25-37.

15. Hibbit, H. D.: "Some Properties of Singular Isoparametric Elements," Int. Journal of Numerical Methods in Engineering, Vol. 11, 1977, pp. 180-184.

16. Bucknall, C. B.: Toughened Composites. Applied Science Publishers, London, 1977.

17. Whitney, W.; and Andrews, R. D.: "Yielding of Glassy Polymers: Volume Effects," J. Polymer Sci., Vol. 16, 1967, pp. 2981-2990.

18. Sternstein, S. S.; and Ongchin, L.: "Yield Criteria for Plastic Deformation of Glassy High Polymers in General Stress Fields," Am. Chem. Soc., Div. Polym. Prepr. Vol. 10, 1969, pp. 1117-1124.

19. Raghava, R.; Coddell, R. M.; and Yeh, G. S.: "The Macroscopic Yield Behavior of Polymers," J. Material Sci., Vol. 8, 1973, pp.225-232.

20. Carapellucci, L. M.; and Yee A. F.: "The Biaxial Deformation And Yield Behavior of Bisphenol-A Polycarbonate: Effect of Anisotrophy," Polymer Engineering Science, Vol. 26, No. 13, July 1986, pp. 920-930.

APPENDIX A.- DISPLACEMENT BOUNDARY CONDITIONS FOR THE LOCAL MODEL

This appendix describes the displacement boundary conditions used with the local finite element model shown in figure 1(b). This local model represents a typical slice of the interior of the DCB specimen in figure 1(a). The boundary displacements for the local model were calculated from a 3D finite element analysis of this DCB specimen. The fiber and resin properties (with a fiber volume ratio of 0.63) used in the fiber-resin model were equivalent to the homogeneous, orthotropic properties used in the 3D analysis. Details of this global analysis are given in reference 11. Only the displacements needed as boundary condition for the local model are presented here.

The u- and v-displacements varied very little across the middle half of the 3D model (less than 0.05 percent for u-displacements and 0.4 percent for v-displacements). Therefore, these displacements were assumed to be constant over the local model thickness. Figures 14(a) and (b) show the distributions of u and v, respectively, for the top edge of the local model. Each of these displacement distributions was fit by a cubic spline interpolation. The resulting equations were then evaluated for each finite element node on the top edge to establish the nodal displacement. The u- and v-displacements for the ends of the model are shown in figures 14(c) and (d). On the bottom edge of the model, v was zero ahead of the delamination front; behind the delamination front, the surface was stress free. Because of the symmetry of the square array of fibers, u- and v-displacement boundary conditions were not needed for the back face (z = 0) or the front face (z = 4 μm) of the local model.

Because of symmetry, the w-displacement on the back face was zero. The w-displacements on the front face were found to vary by less than six percent from an average value of $-0.81 \times 10^{-3} \mu m$ found from the 3D DCB analysis. Furthermore, because this value was three orders of magnitude less than the u-displacements and two orders of magnitude less than the v-displacements, this average w-displacement was imposed on the front face.

Because the w-displacements were nearly uniform over the local model, its 3D stress state could be approximated as generalized plain strain. As a result, the local model could have been analyzed using generalized plain strain boundary conditions without significant error.

APPENDIX B - A MODIFIED VON MISES YIELD CRITERION

The yielding of materials under multi-axial stress can be predicted by the following form of the von Mises yield criterion.

$$\frac{\frac{3}{\sqrt{2}} \tau_{oct}}{\sigma_{ys}} = 1 \tag{B1}$$

Here τ_{oct} is the octahedral shear stress and σ_{ys} is the uniaxial yield stress in tension. Equation (B1) was developed from a distortional energy analysis and assumes that the hydrostatic stress σ_{m} has no influence on yielding. For metallic materials this appears to be reasonably accurate. However, for thermoplastic polymers, yielding is sensitive to the hydrostatic stress [16-20]. A hydrostatic compression stress increases the resistance to yielding, while a hydrostatic tensile stress decreases the resistance. Sternstein and Ongchin [18] suggested a modification to equation (B1) to include the effects of the hydrostatic stress. The modified equation is

$$\frac{a_1 \tau_{oct} + a_2 \sigma_m}{\sigma_{ys}} = 1 \tag{B2}$$

This equation is referred to herein as the modified von Mises yield criterion. The constants a_1 and a_2 were obtained by fitting equation (B2) to the test data reported in references 17 through 20 for various thermoplastic resins. Figure 15 shows a plot of the octahedral shear stress (normalized by the uniaxial yield stress in tension) as a function of the normalized hydrostatic stress for four polymers: polyvinyl chloride (PVC), polystyrene (PS), polycarbonate (PC), and polymethyl methacrylate (PMMA). Using a linear

20

regression analysis, the constants a_1 and a_2 were found to be 1.91 and 0.30, respectively. The resulting equation is shown in figure 15 as a solid line. If the hydrostatic component had no effect on yielding, the line would be horizontal. The negative slope shows that tensile hydrostatic stresses tend to reduce the octahedral stress corresponding to yielding. Equation (B2) reduces to equation (B1) for the uniaxial case, where $\sigma_m = \sigma_{ys}/3$.

Table 1.- Elastic material properties for graphite/epoxy.

Elastic Constants[a]	Fiber	Resin [11]	Lamina [11]
E_{11}, GPa	211	3.4	134
E_{22}, GPa	42.0	3.4	13.0
E_{33}, GPa	42.0	3.4	13.0
G_{12}, GPa	120	1.3	6.4
G_{13}, GPa	120	1.3	6.4
G_{23}, GPa	14.5	1.3	4.8
ν_{12}	0.36	0.30	0.34
ν_{13}	0.36	0.30	0.34
ν_{23}	0.45	0.30	0.35

[a] 1, 2, and 3 refer to fiber, transverse, and thickness
directions, respectively.

Local model region (not to scale)

w

x

24h

Resin interface layer

y

z

P

P

a

(a) DCB model

Homogeneous region

x

z

Fiber–resin region (see figure 2)

y

165

165

165

4

135 (h)
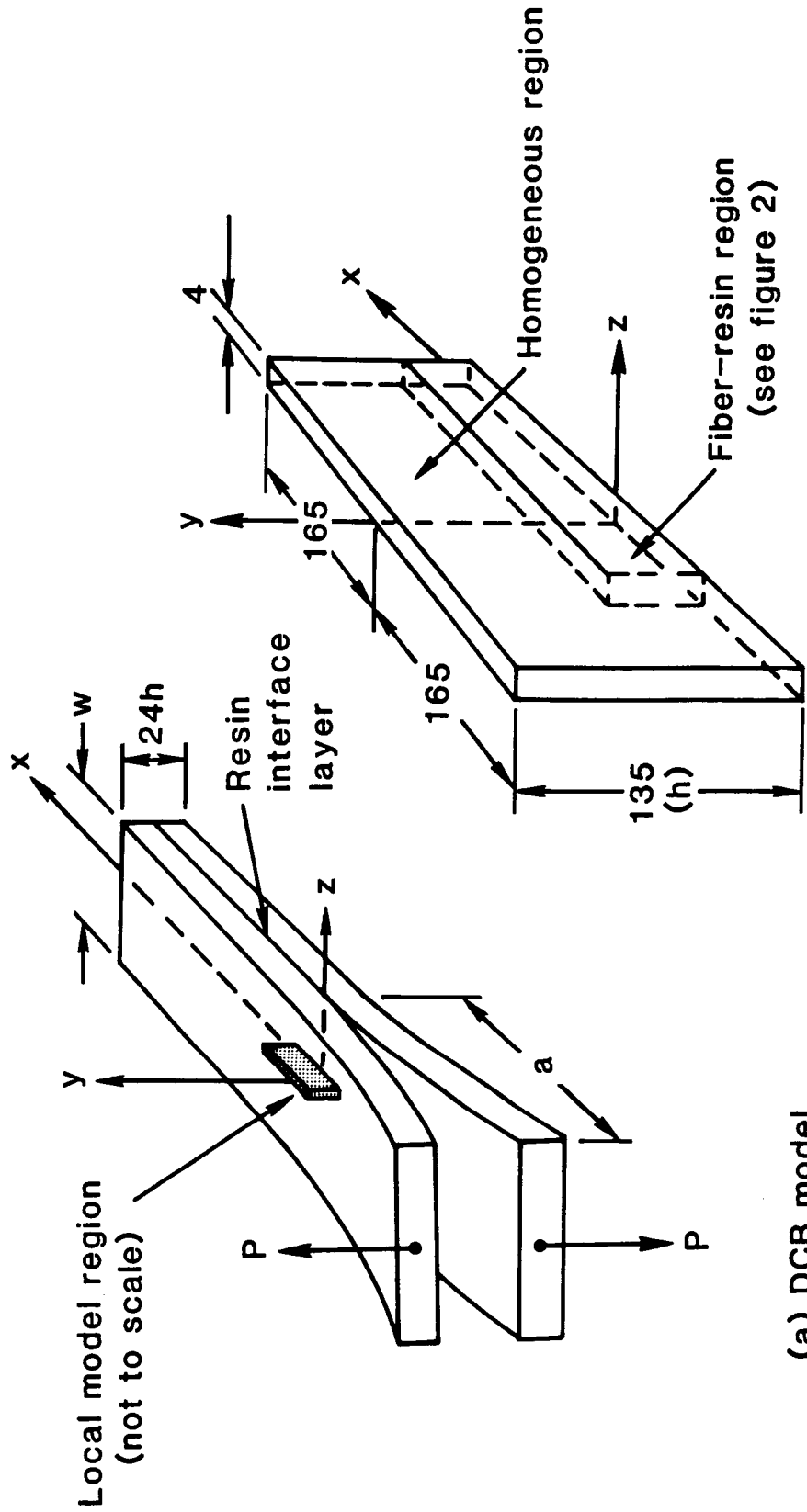
(b) Local model

Figure 1.- DCB specimen configuration, loading, and local model (all dimensions in μm).

Delamination front

z

.05

.75

(b) Detail near delamination front

x

z

Resin layer

165

y

80

t/2 = 5

4

37
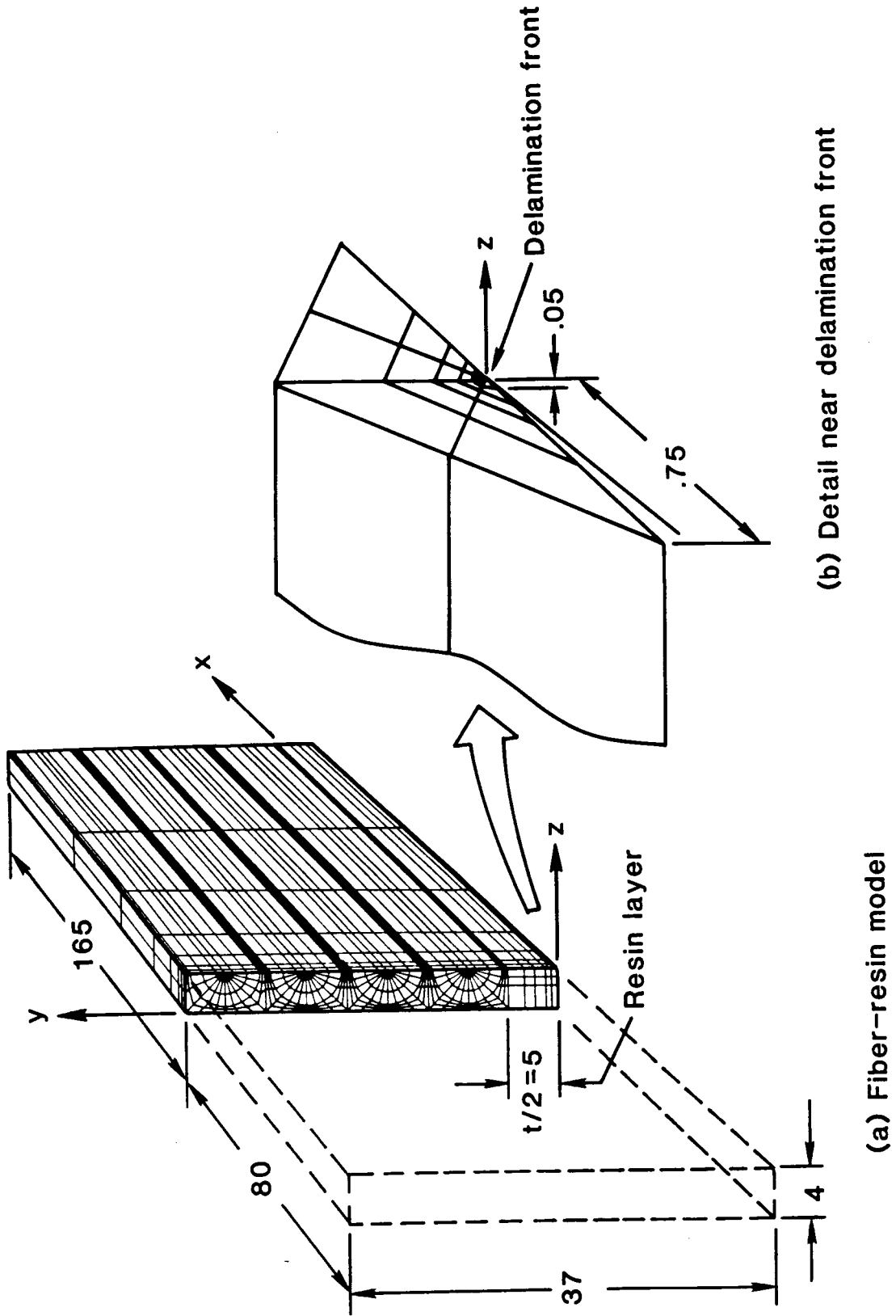
(a) Fiber-resin model

Figure 2.- Local fiber-resin finite element model (all dimensions in μm).
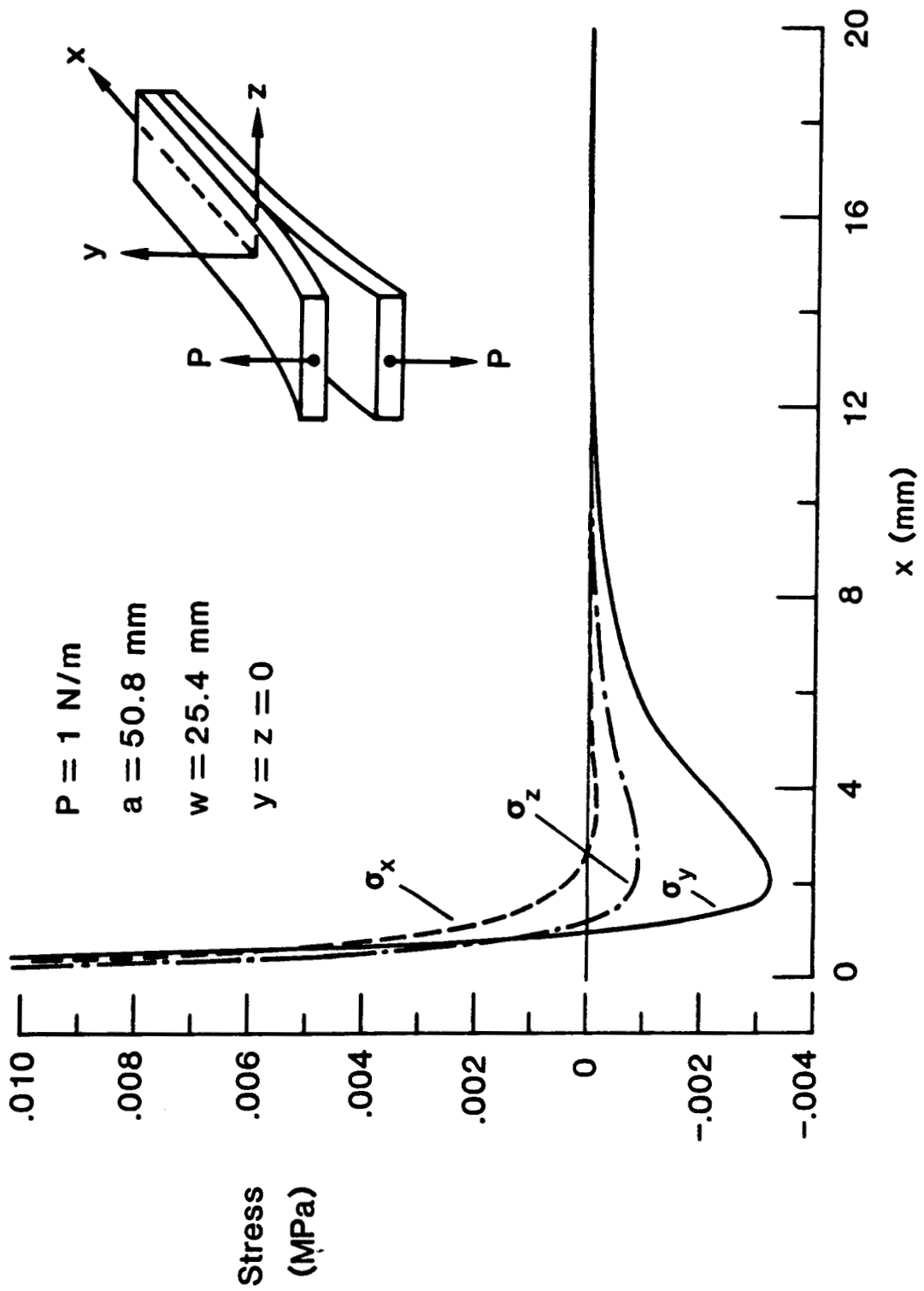
Figure 3.- Stress distributions along the x-axis ahead of the delamination for the 3D orthotropic, homogeneous model [11].
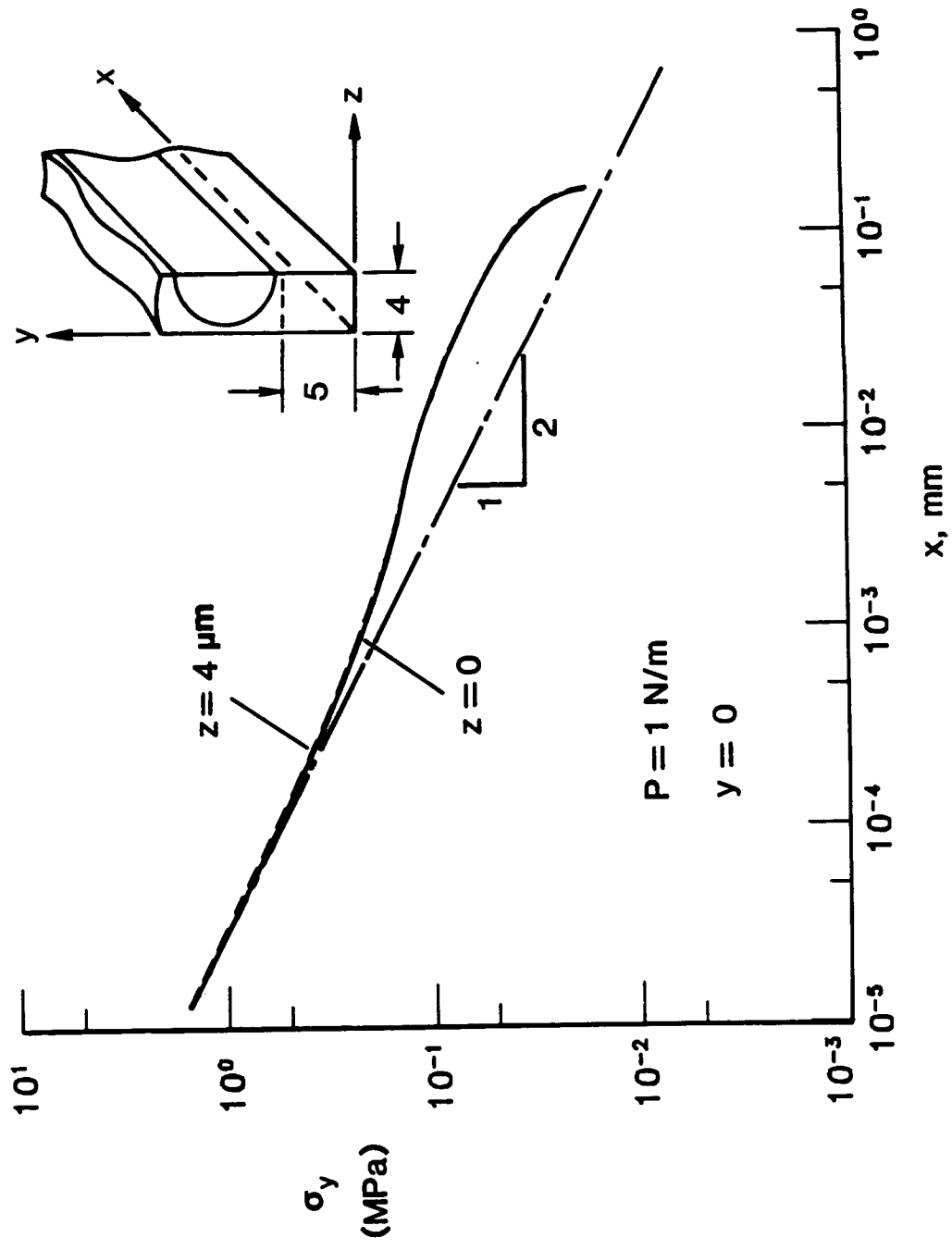
Figure 4.- The σ_y stress distribution ahead of the delamination.
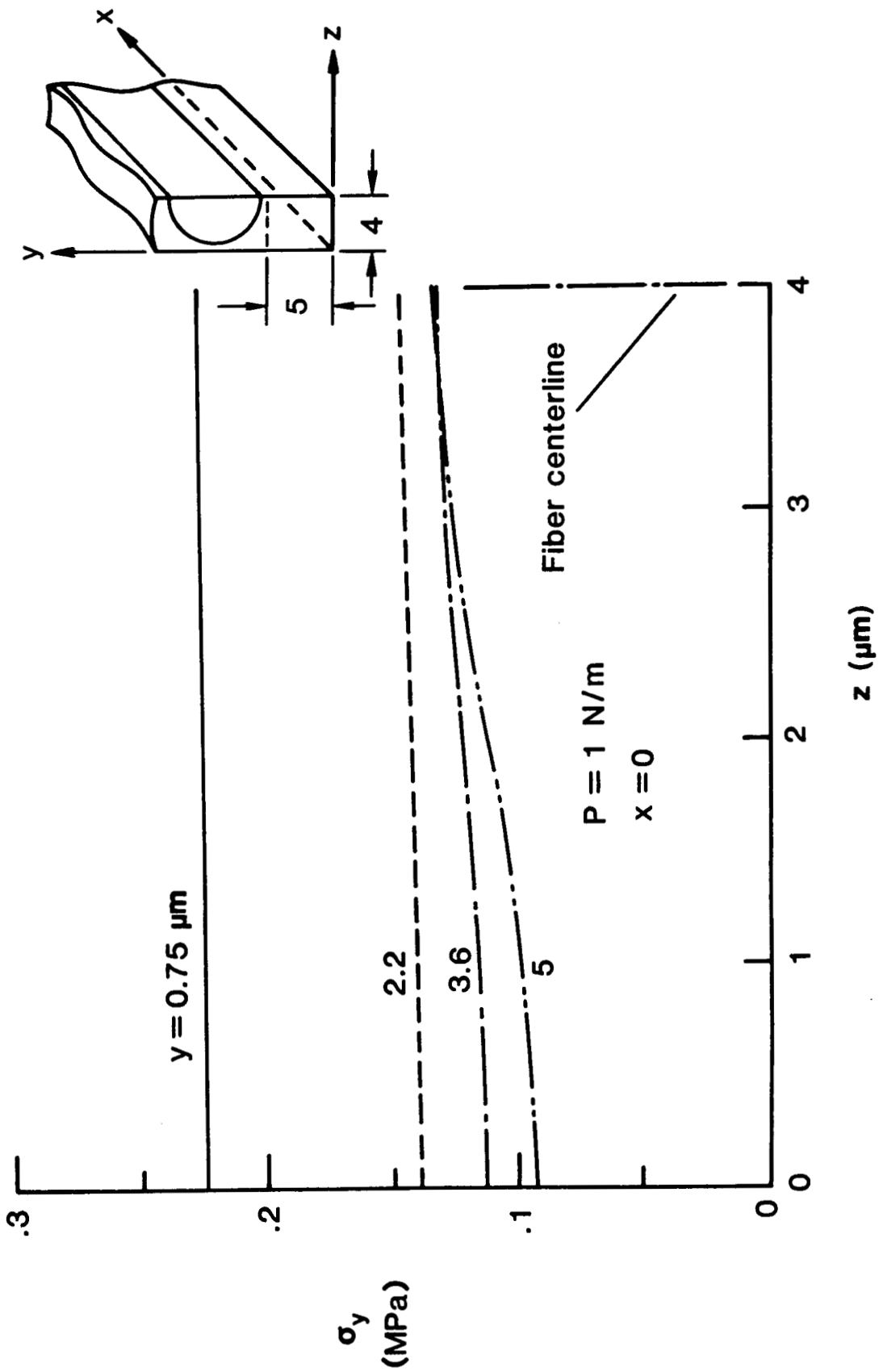
Figure 5. - Distributions of σ_y in the resin layer above the delamination front.
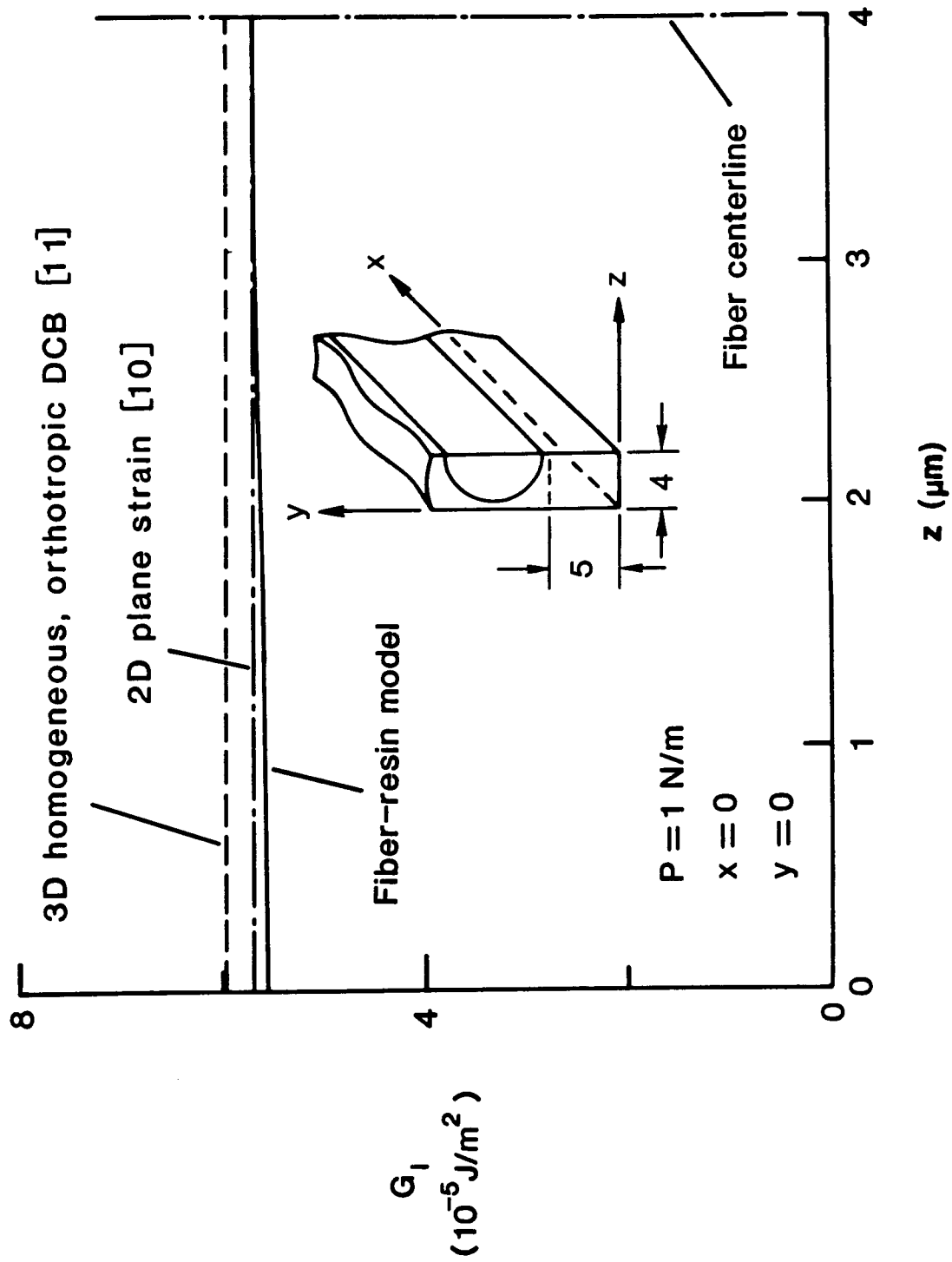
Figure 6.- Comparison of strain-energy-release rates along the delamination front.
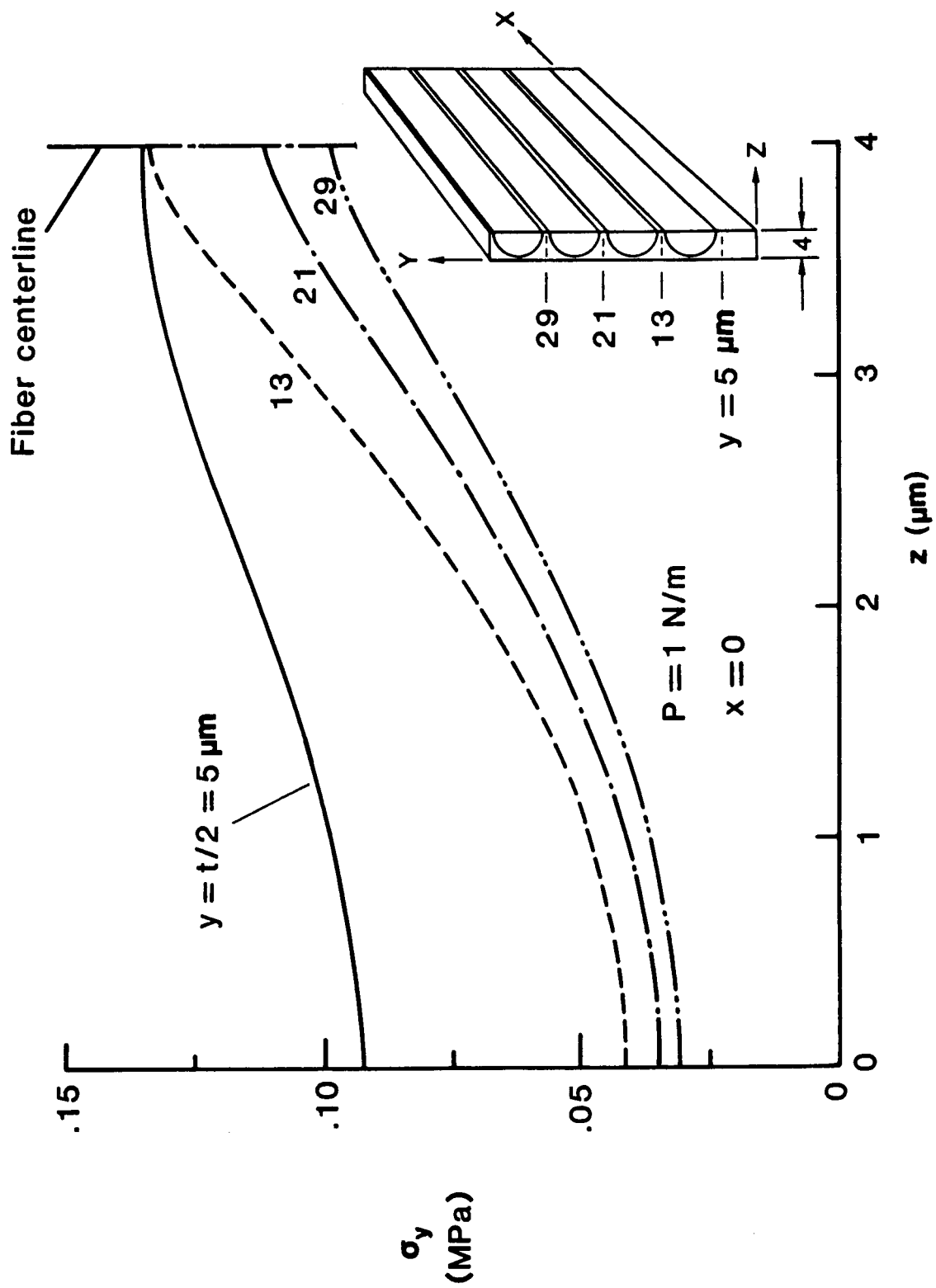
Figure 7.- Distributions of σ_y between the fibers in the z-direction.
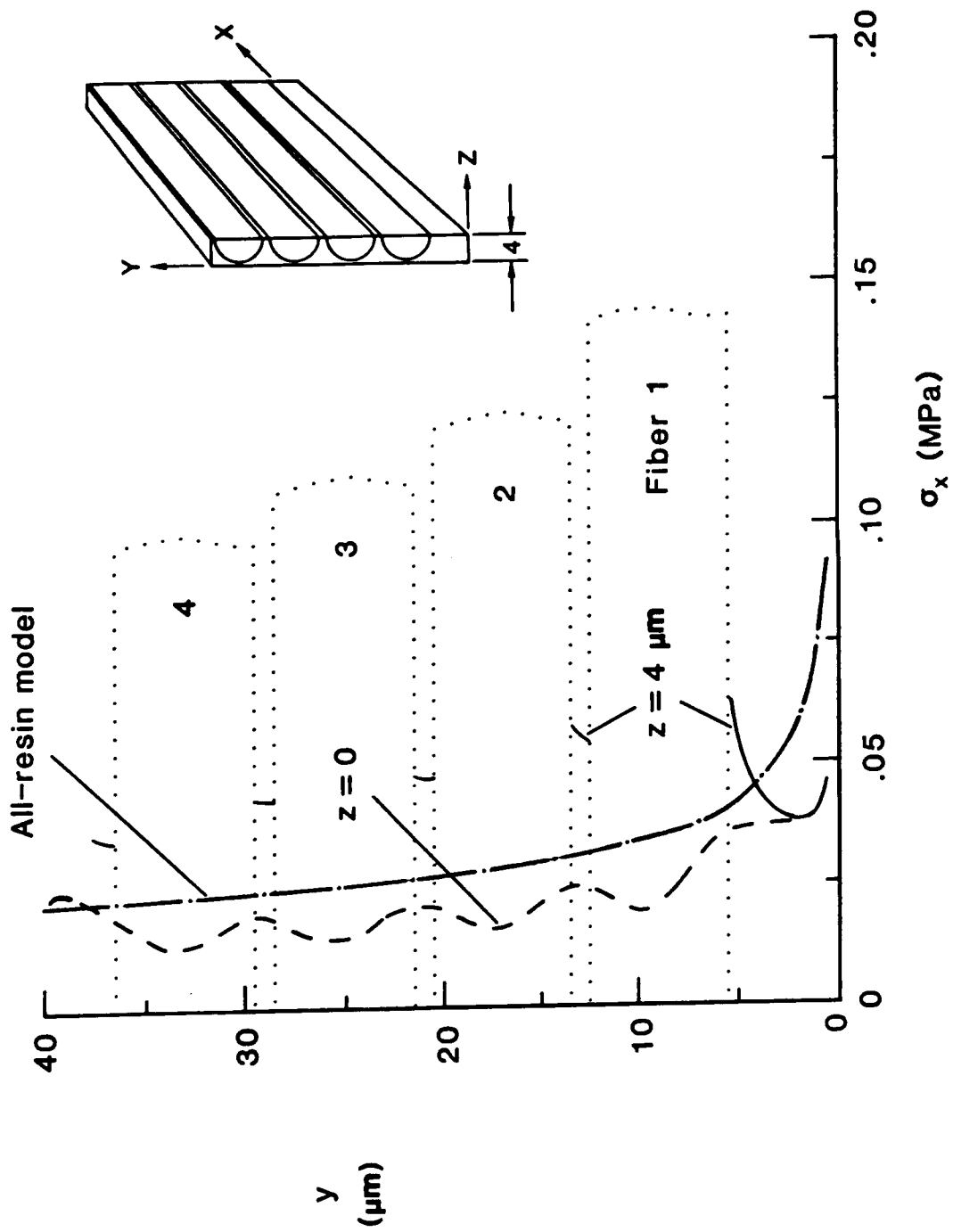
(a) σ_x stress distributions

Figure 8.- Ply stress distributions in the y-direction above the delamination front.
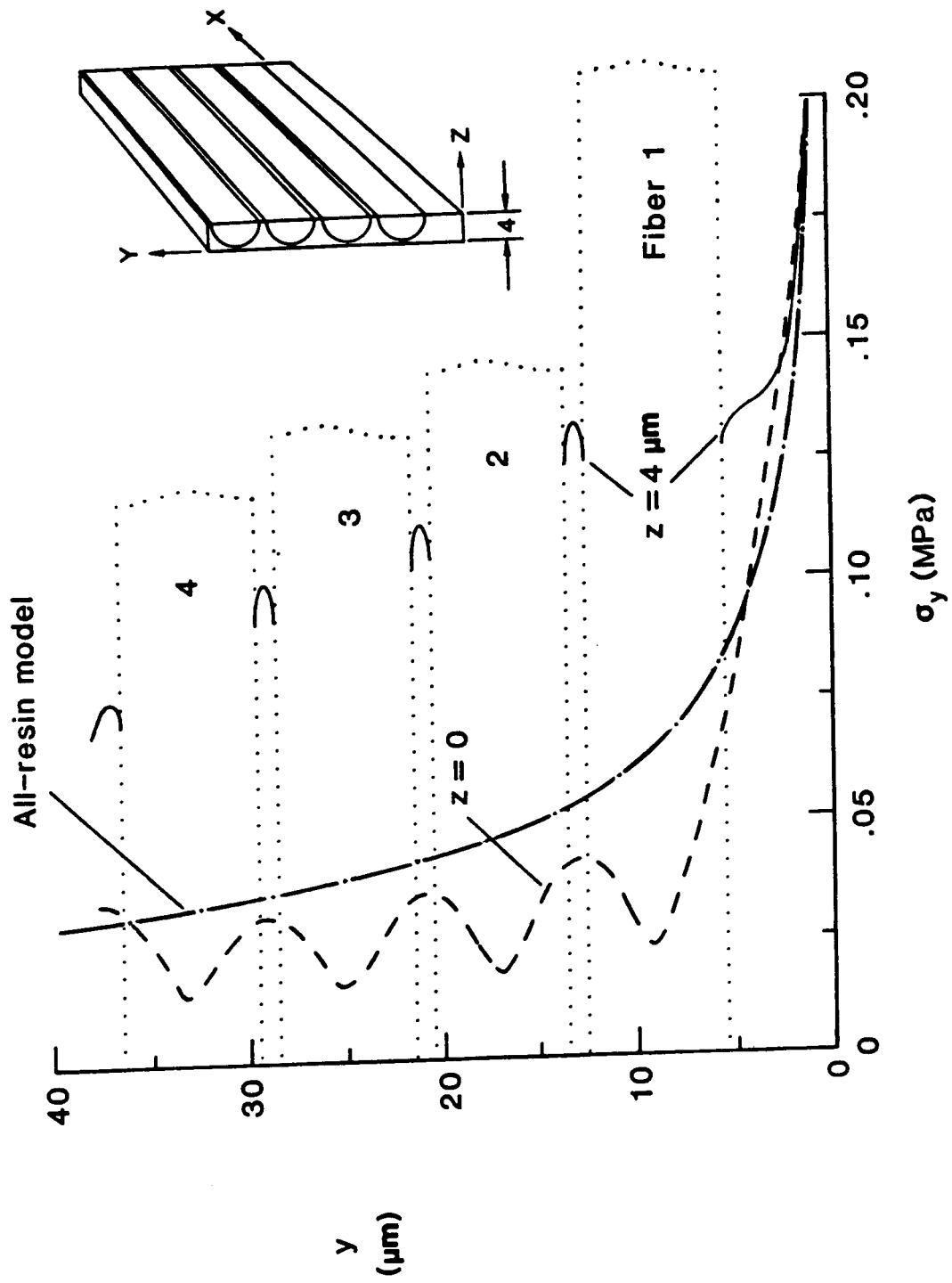
(b) σ_y stress distributions

Figure 8. - Continued.

31
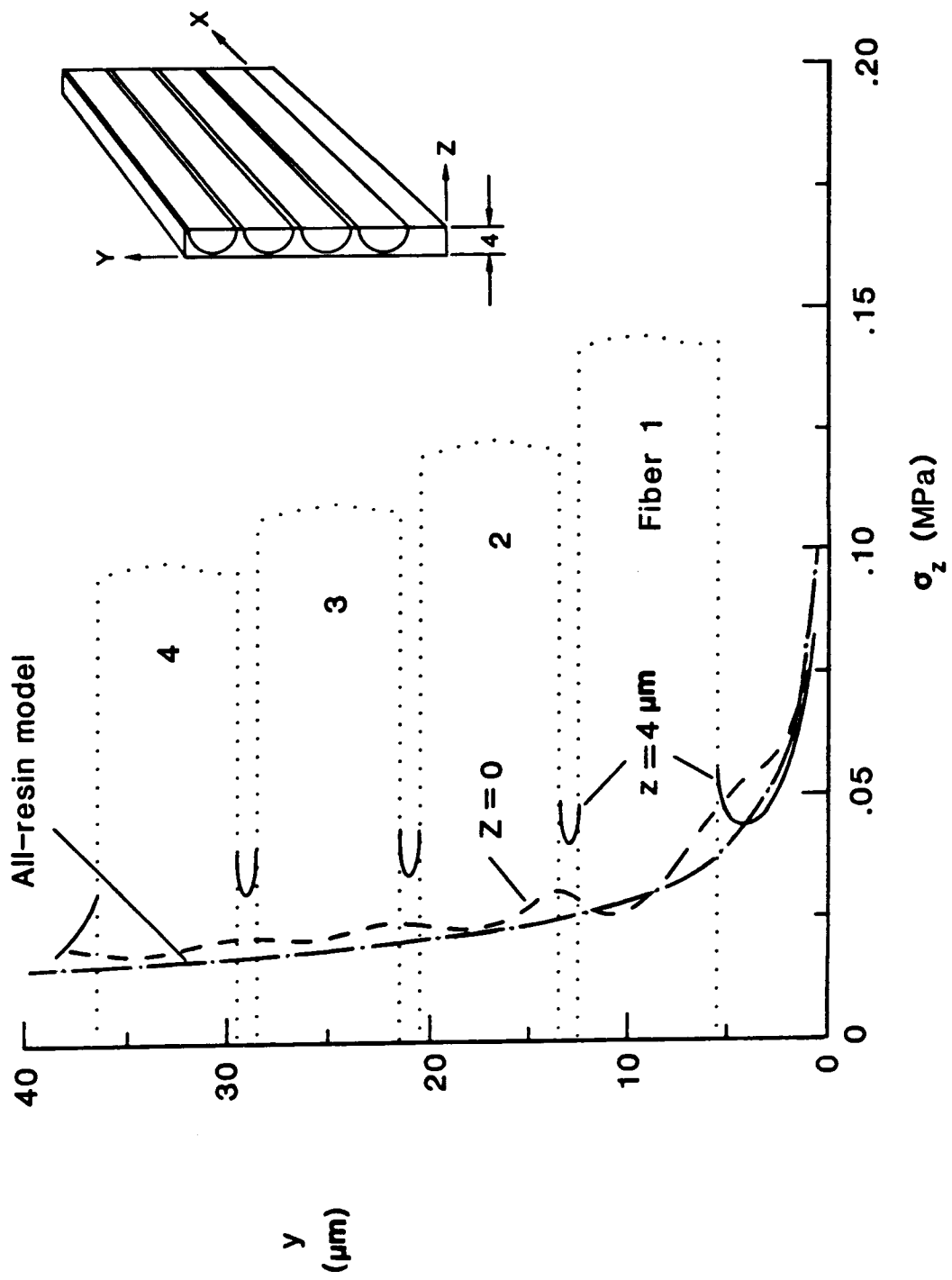
(c) σ_z stress distributions

Figure 8. - Concluded.
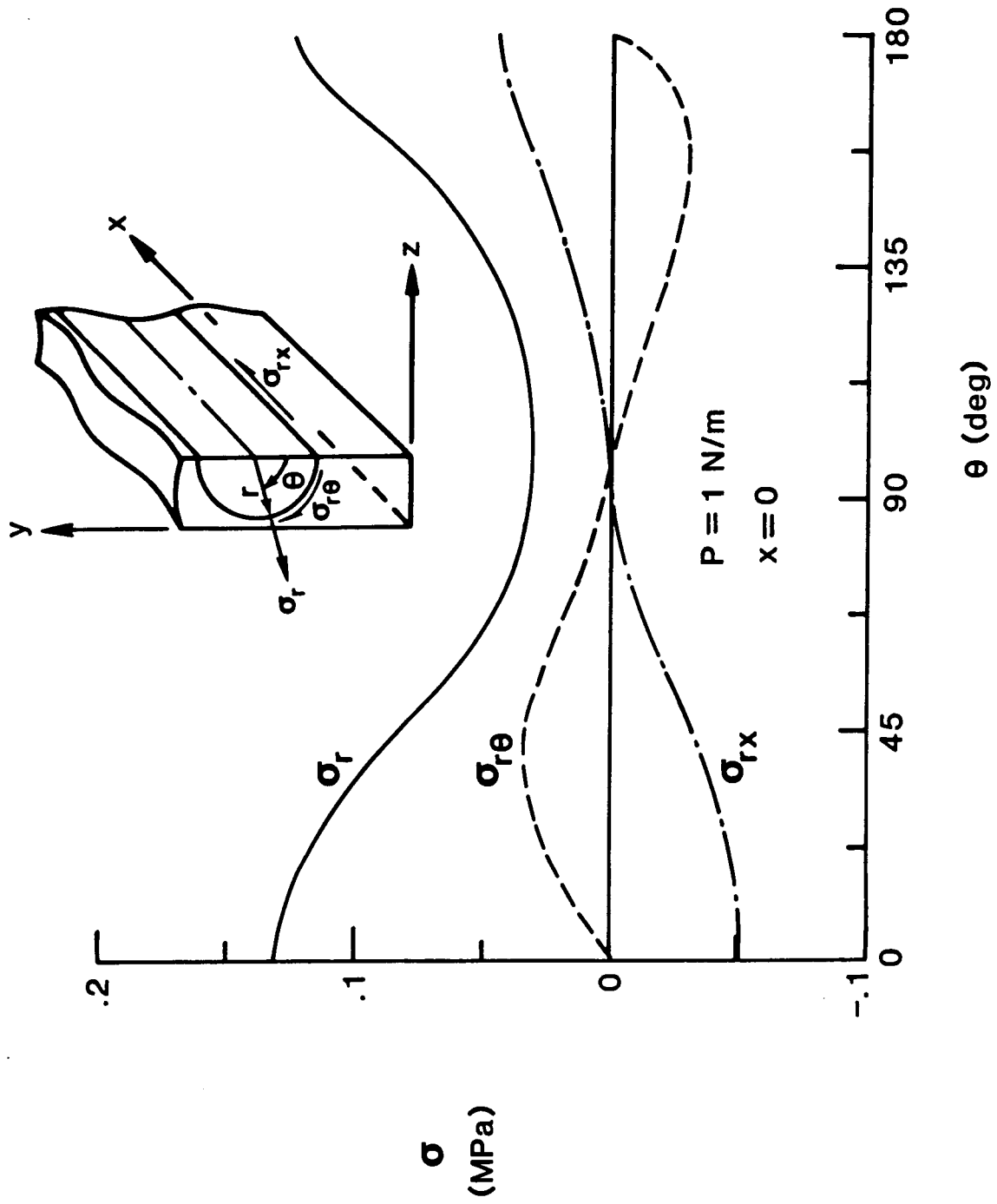
Figure 9.- Fiber-resin interface stresses in the first fiber above the delamination front (in the x = 0 plane).

33
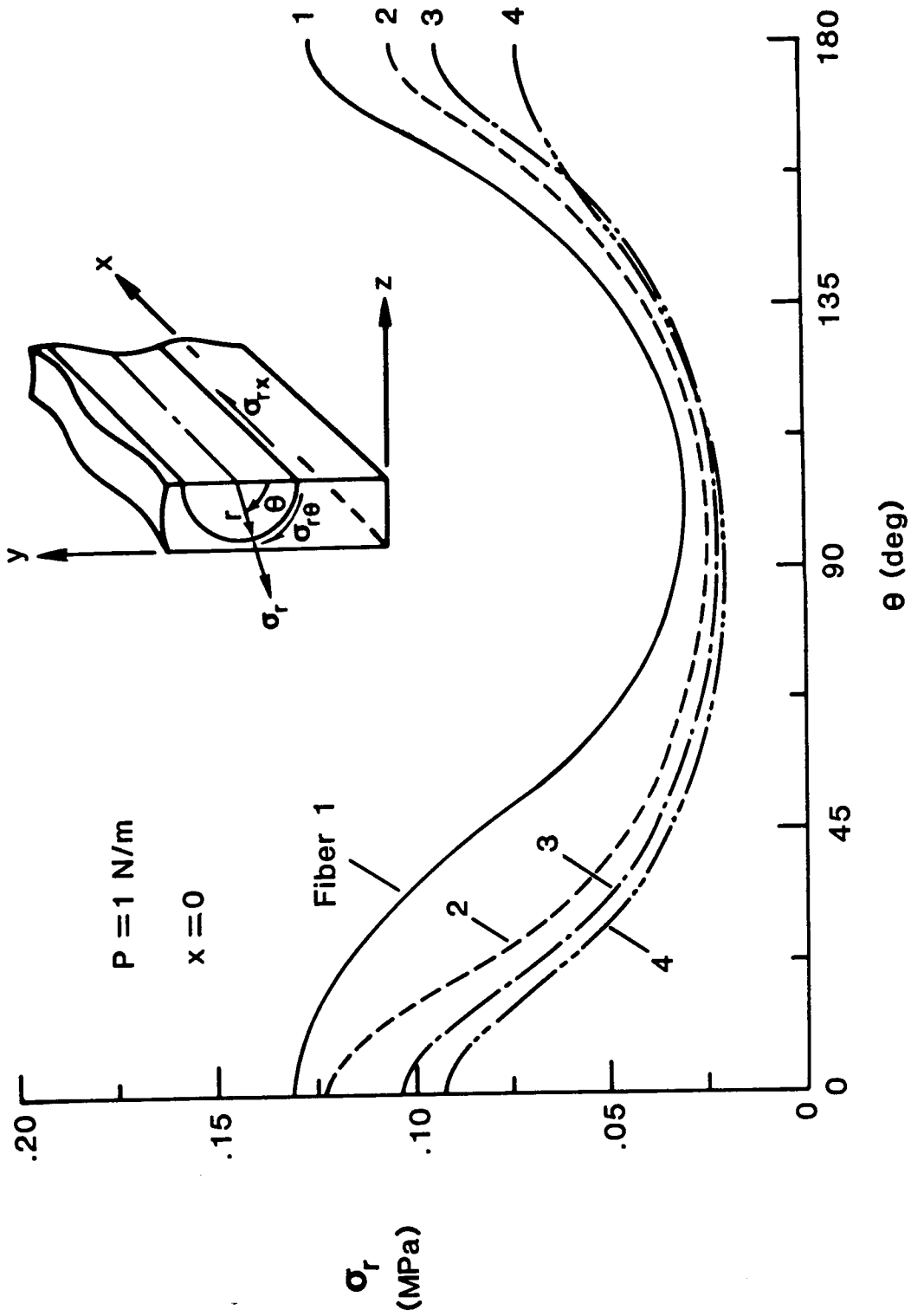
(a) σ_r stress distributions

Figure 10.- Fiber-resin interface stresses for the $x = 0$ plane.
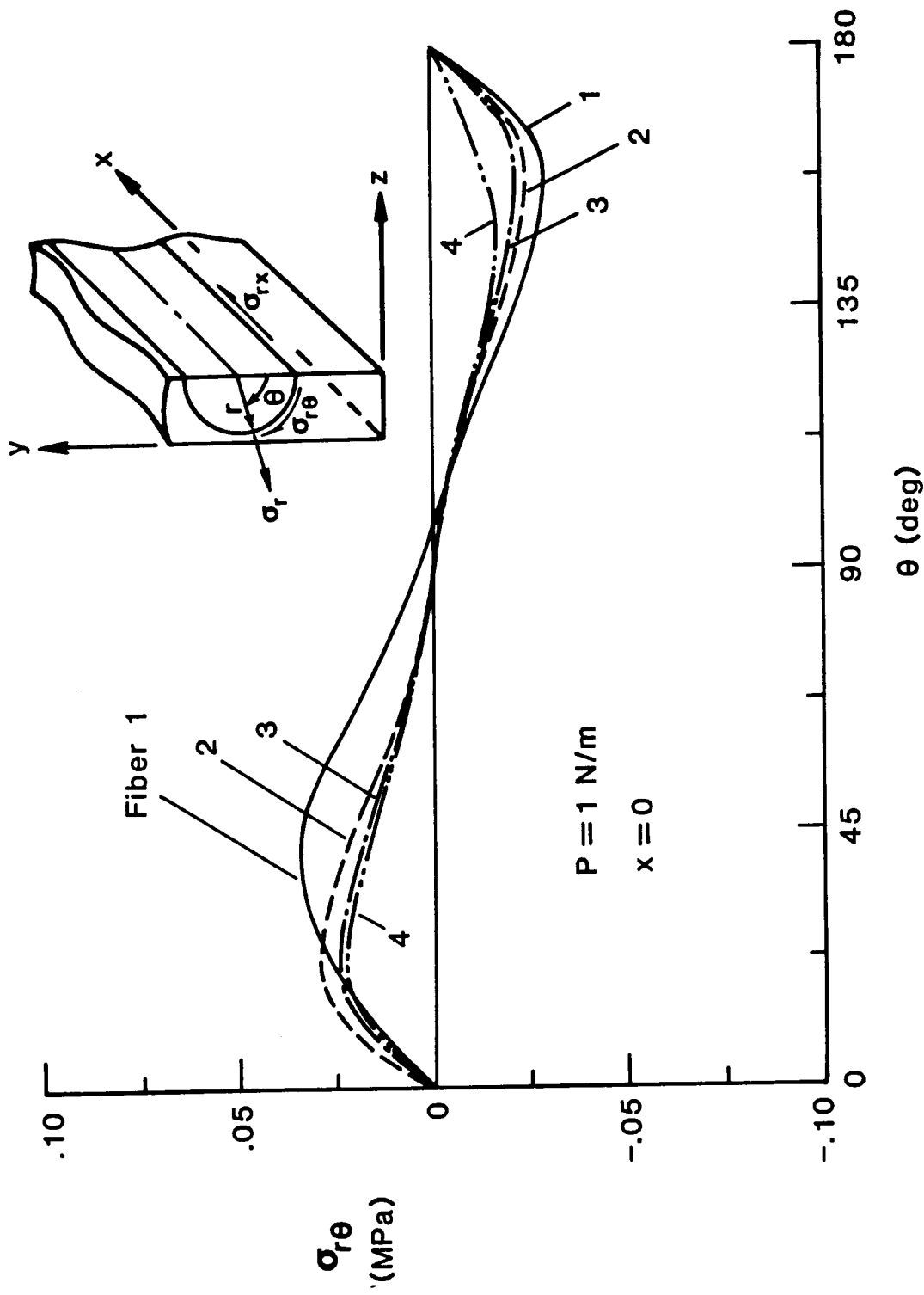
(b) $\sigma_{r\theta}$ stress distributions

Figure 10. - Continued.
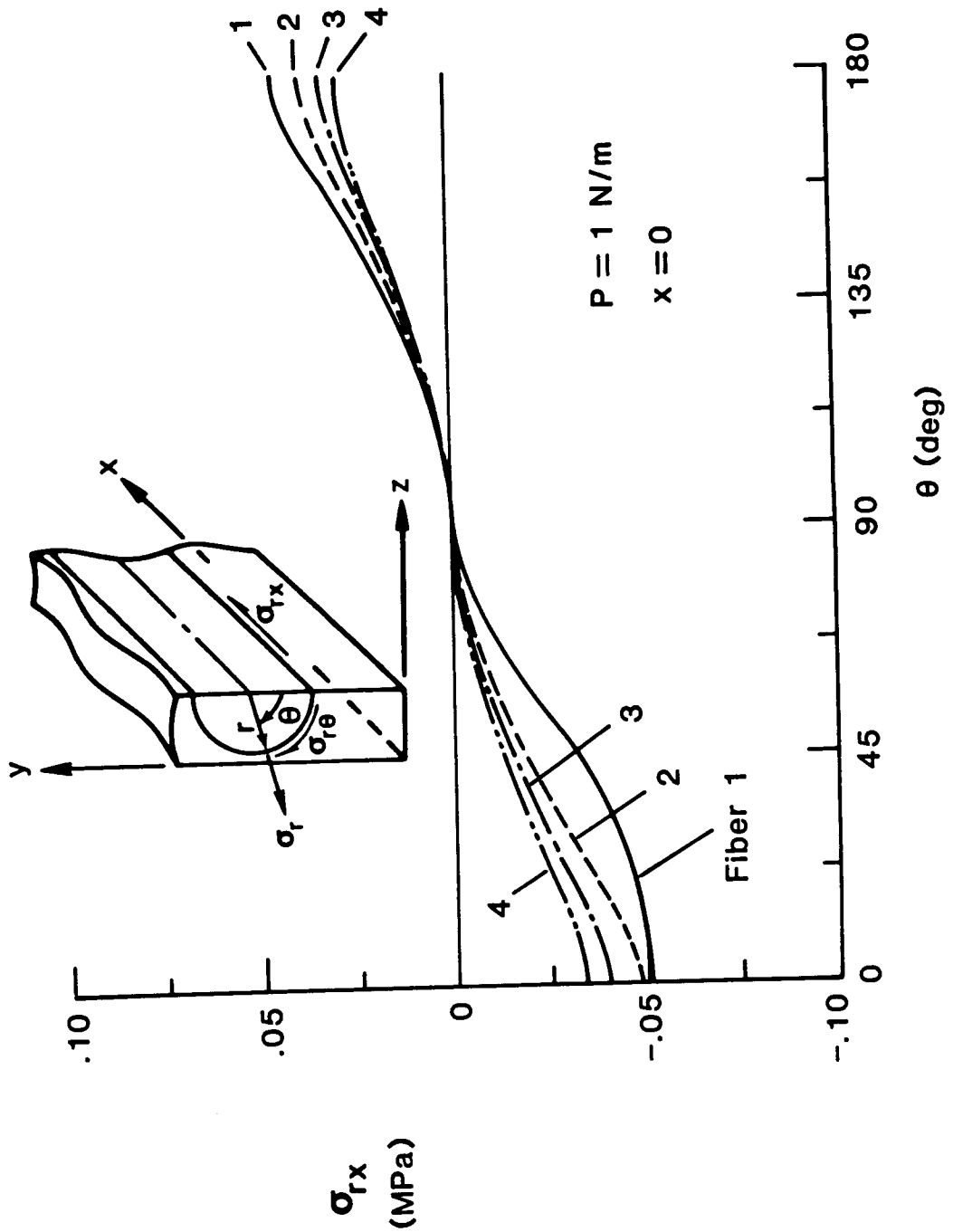
(c) σ_{rx} stress distributions

Figure 10. - Concluded.
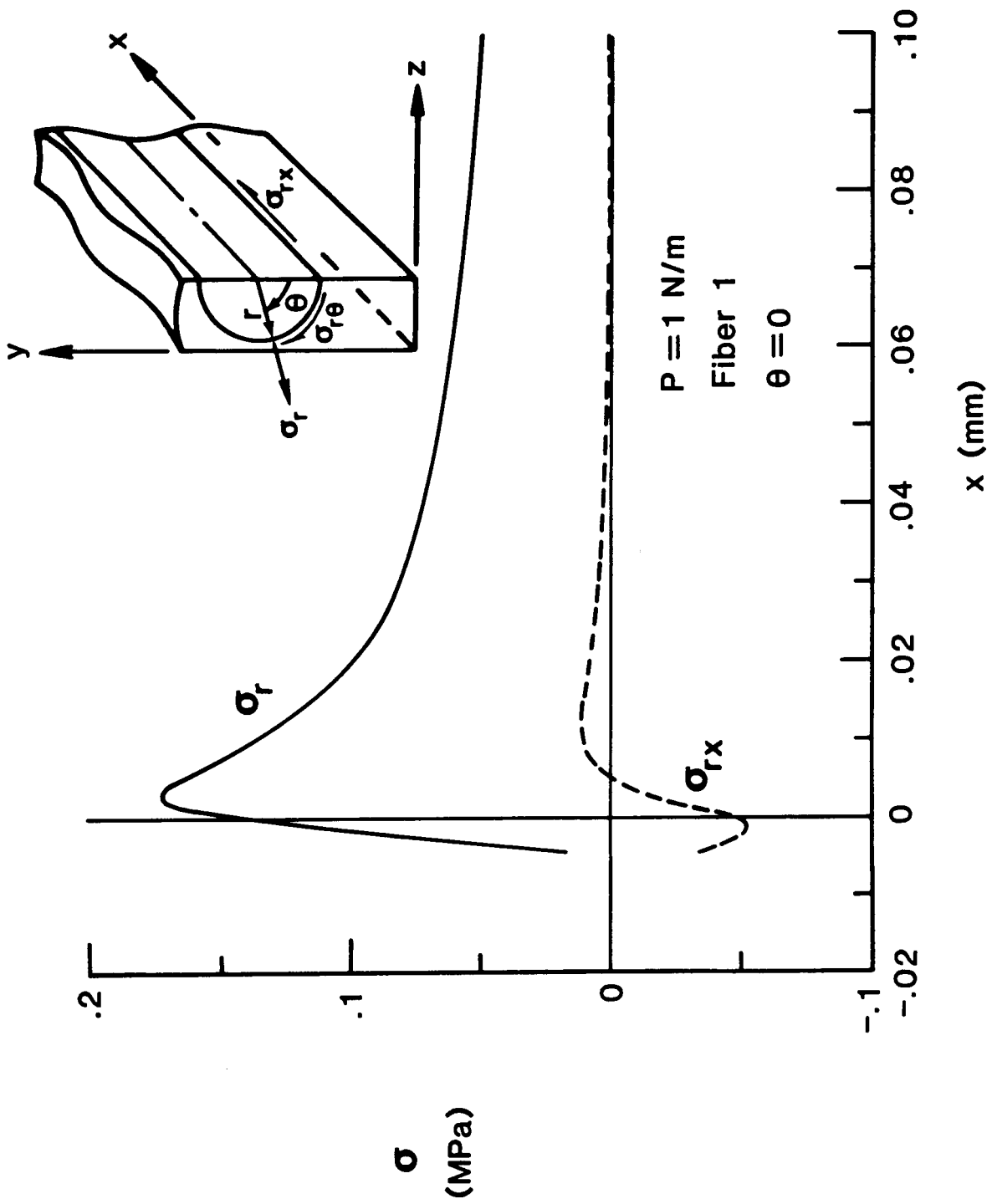
Figure 11.- Fiber-resin interface stresses along the first fiber.

Shading indicates yielding
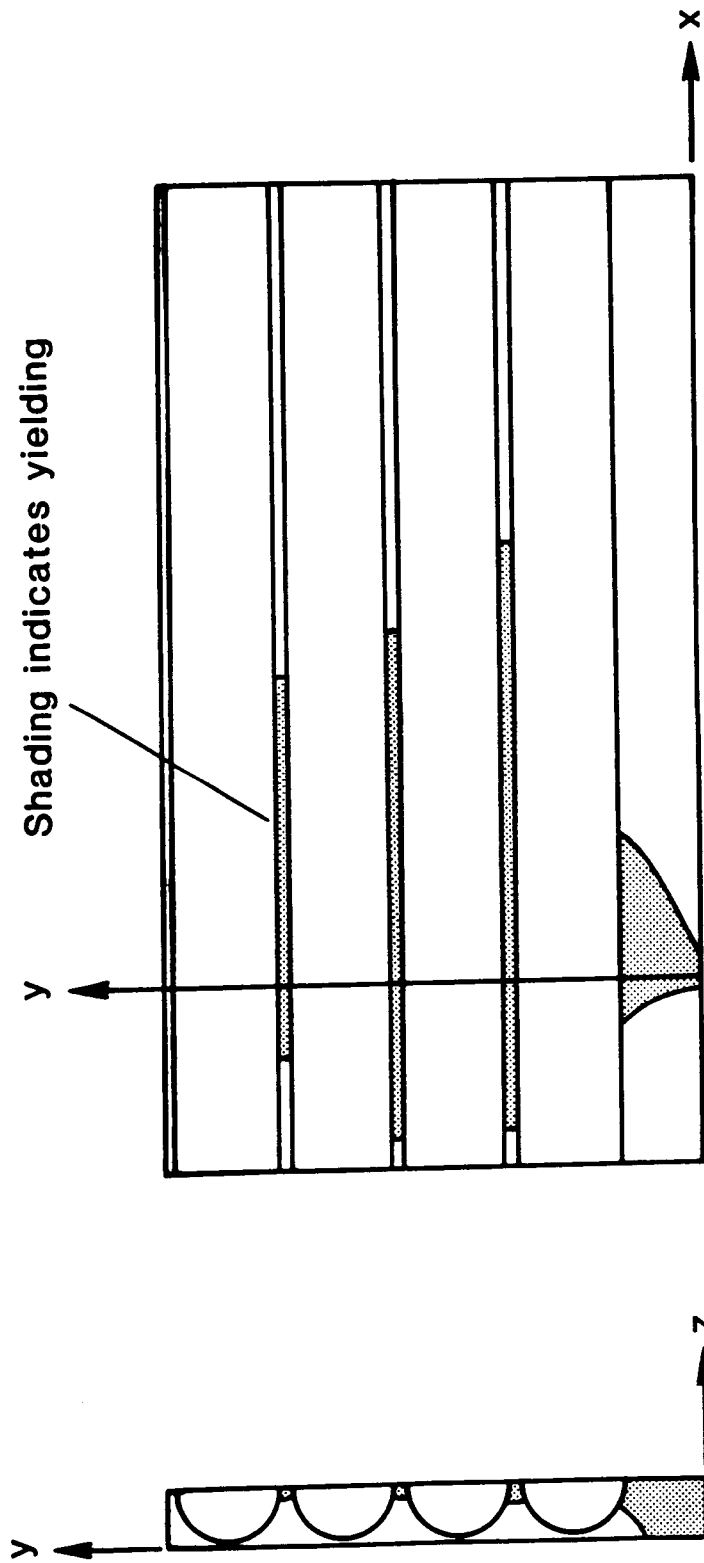
(a) x = 0 plane

(b) z = 4 μm plane (front surface of model)

Figure 12.- Yield zone estimates based on the von Mises yield criterion.

38
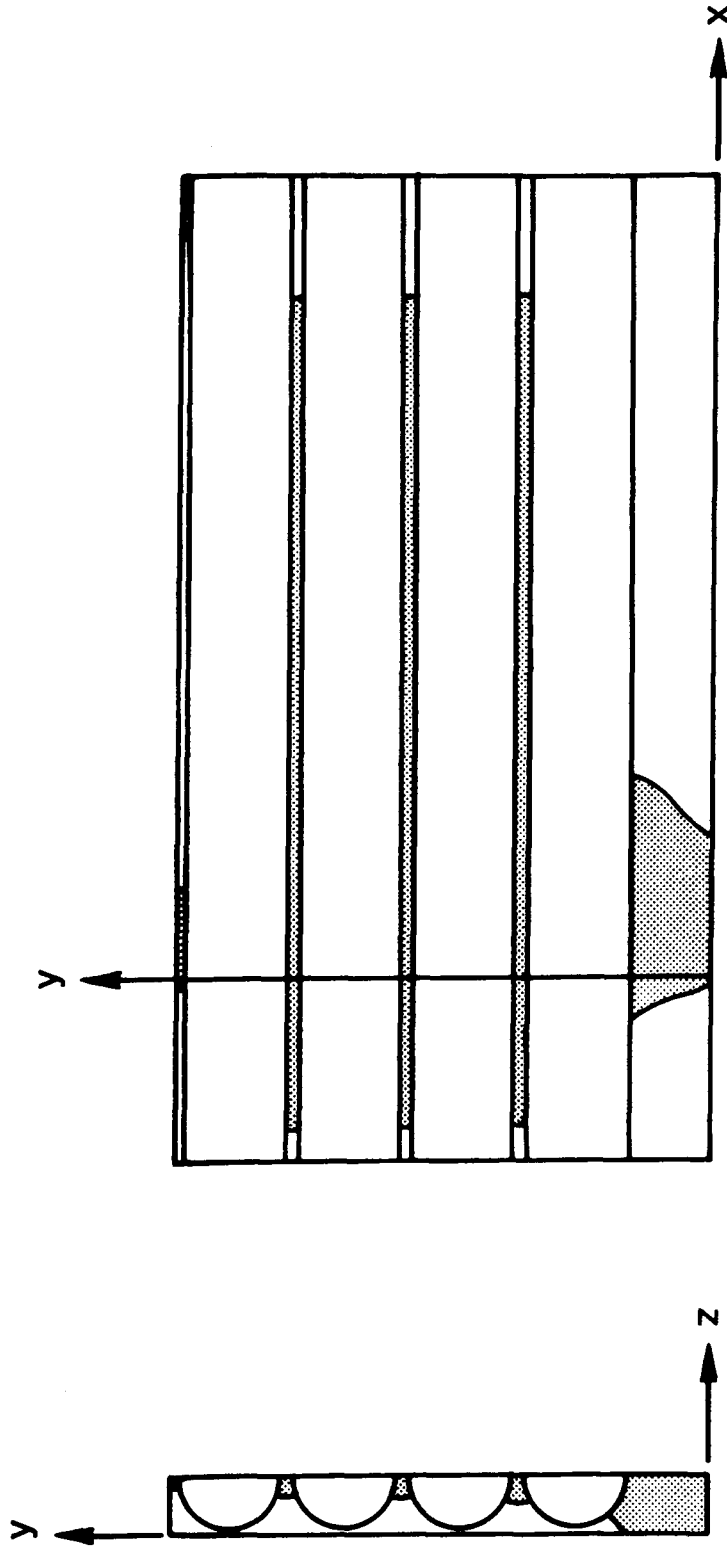
(a) x = 0 plane   (b) z = 4 μm plane (front surface of model)

Figure 13.- Yield zone estimates based on a modified von Mises yield criterion that accounts for hydrostatic stress effects.
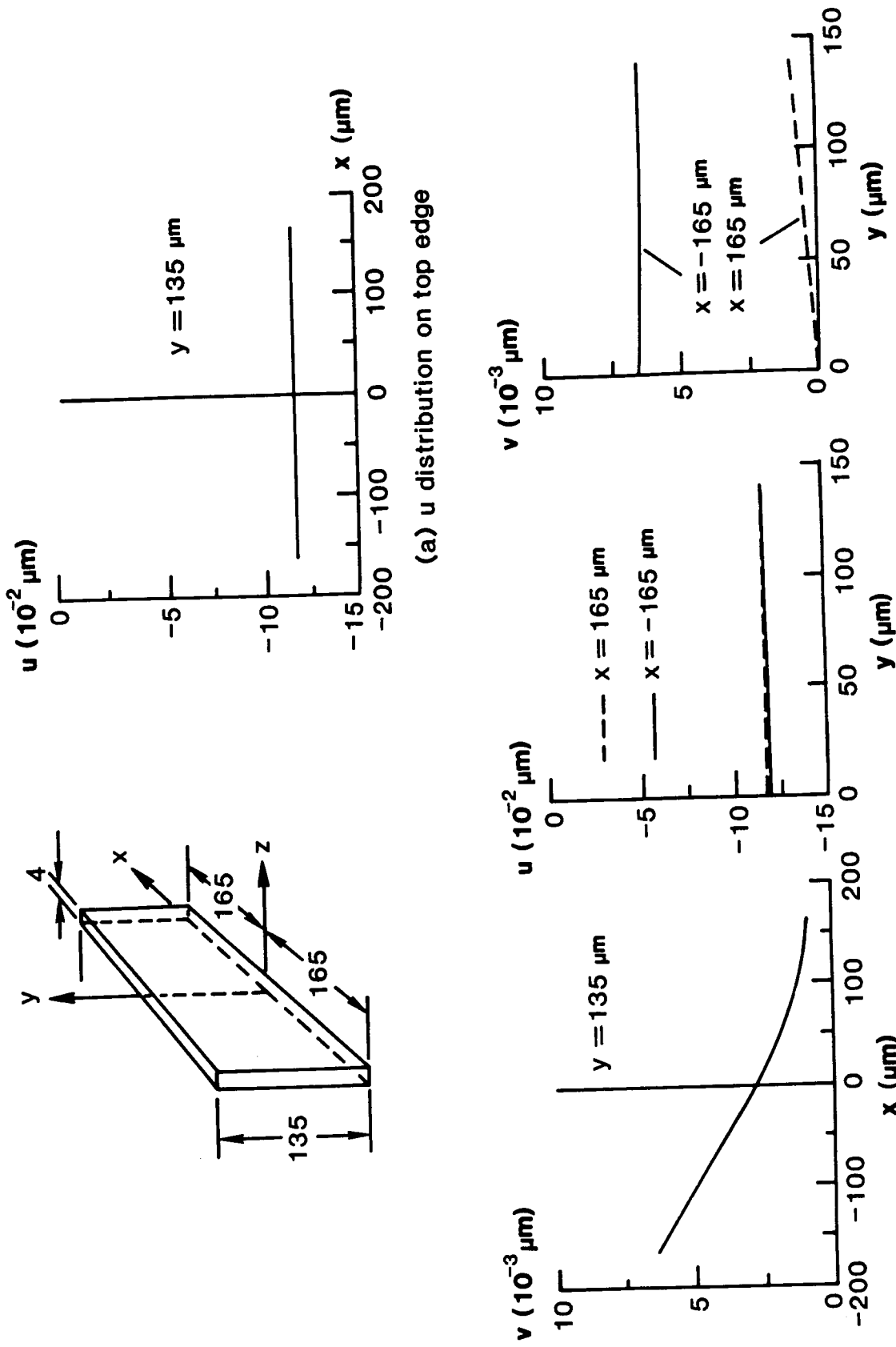
Figure 14.- Displacement boundary conditions for the local finite element model.
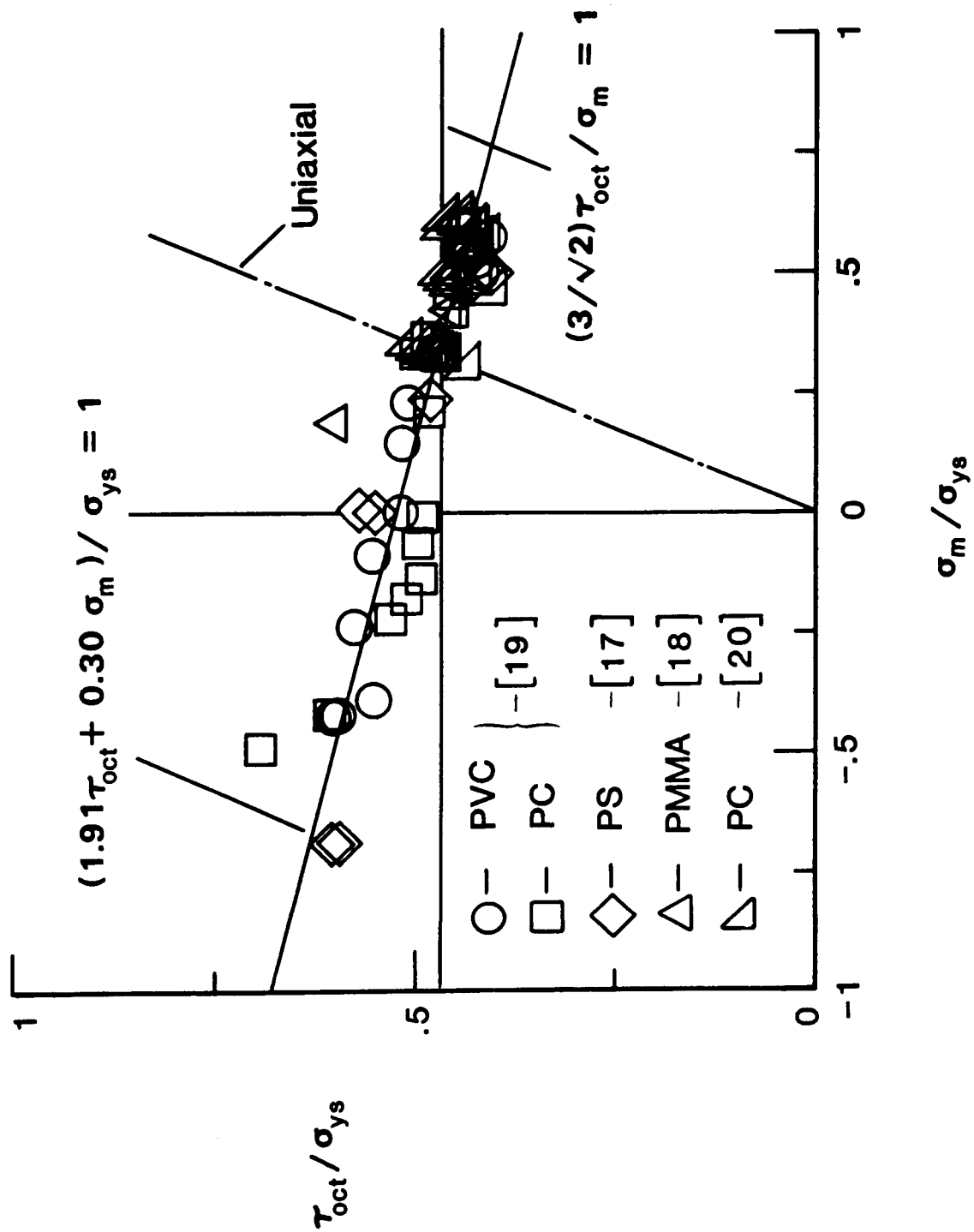
Figure 15.- Effects of hydrostatic stress on yielding of thermoplastic resins.

Standard Bibliographic Page

1. Report No. NASA TM-100540	2. Government Accession No.	3. Recipient's Catalog No.
4. Title and Subtitle A FIBER-RESIN MICROMECHANICS ANALYSIS OF THE DELAMINATION FRONT IN A DCB SPECIMEN		5. Report Date January 1988
		6. Performing Organization Code
7. Author(s) J. H. Crews, Jr.; K. N. Shivakumar*; and I. S. Raju*		8. Performing Organization Report No.
9. Performing Organization Name and Address NASA Langley Research Center Hampton, VA 23665-5225		10. Work Unit No. 505-63-01-05
		11. Contract or Grant No.
12. Sponsoring Agency Name and Address National Aeronautics and Space Administration Washington, DC 20546		13. Type of Report and Period Covered Technical Memorandum
		14. Sponsoring Agency Code

15. Supplementary Notes

*K. N. Shivakumar and I. S. Raju, Analytical Services & Materials, Inc., 28 Research Drive, Hampton, VA

16. Abstract

A three-dimensional (3D) finite-element model was developed to analyze the fiber-resin behavior near the delamination front in a graphite/epoxy double cantilever beam (DCB) specimen. The specimen interior was analyzed using a typical "one-fiber slice," represented by a local 3D fiber-resin model. The resin stresses were computed for the resin-rich layer at the ply interface as well as for the regions between and around the fibers. Stress concentrations were found between the fibers close to the delamination front. However, the computed strain energy release rate G_I along the delamination front varied by less than two percent, and was within about four percent of the plane-strain value.

The von Mises yield criterion was used to estimate the extent of yielding near the the delamination front. The yielding extended ahead of the delamination and also developed between the fibers. Although the fibers had only a negligible effect on G_I, they caused yielding within the ply and therefore could influence delamination fracture toughness.

The normal and shear stresses at the fiber-resin interface were computed near the delamination front. These results suggest that multi-axial stress criteria may be required to analyze fiber-resin interfaces.

17. Key Words (Suggested by Authors(s)) Composites Micromechanics Delamination Yielding Fiber-resin interface	18. Distribution Statement Unclassified - Unlimited Subject Category - 24		
19. Security Classif.(of this report) Unclassified	20. Security Classif.(of this page) Unclassified	21. No. of Pages 42	22. Price A03

NASA Langley Form 63 (June 1985)